

Emergent Magnetic Fan Structures in Manganite Homostructure Arrays

Laura Guasco,* Yury Khaydukov, Gideok Kim, Thomas Keller, Alexei Vorobiev, Anton Devishvili, Peter Wochner, Georg Christiani, Gennady Logvenov, and Bernhard Keimer

Devices with tunable magnetic noncollinearity are important components of superconducting electronics and spintronics, but they typically require epitaxial integration of several complex materials. The spin-polarized neutron reflectometry measurements on $\text{La}_{1-x}\text{Sr}_x\text{MnO}_3$ homostructure arrays with modulated Sr concentration reported herein have led to the discovery of magnetic fan structures with highly noncollinear alignment of Mn spins and an emergent periodicity twice as large as the array's unit cell. The neutron data show that these magnetic superstructures can be fully long-range ordered, despite the gradual modulation of the doping level created by charge transfer and chemical intermixing. The degree of noncollinearity can be effectively adjusted by low magnetic fields. Notwithstanding their chemical and structural simplicity, oxide homostructures thus show considerable promise as a platform for tunable complex magnetism and as a powerful design element of spintronic devices.

1. Introduction

Oxide heterojunctions exhibit a large variety of charge, spin, and orbital reconstructions,^[1–10] with multifold potential applications

L. Guasco, Y. Khaydukov, G. Kim, T. Keller, P. Wochner, G. Christiani, G. Logvenov, B. Keimer
 Max-Planck-Institut für Festkörperforschung
 Heisenbergstraße 1, D-70569 Stuttgart, Germany
 E-mail: l.guasco@fkf.mpg.de

L. Guasco, Y. Khaydukov, T. Keller
 Max Planck Society Outstation at the Heinz Maier-Leibnitz Zentrum (MLZ)
 D-85748 Garching, Germany

A. Vorobiev, A. Devishvili
 Institut Laue-Langevin
 71 avenue des Martyrs, CS 20156, Grenoble Cedex 9 F-38042, France

A. Vorobiev, A. Devishvili
 Department of Physics and Astronomy
 Uppsala University
 Box 516, Uppsala 751 20, Sweden

 The ORCID identification number(s) for the author(s) of this article can be found under <https://doi.org/10.1002/adma.202202971>.

© 2022 The Authors. Advanced Materials published by Wiley-VCH GmbH. This is an open access article under the terms of the Creative Commons Attribution License, which permits use, distribution and reproduction in any medium, provided the original work is properly cited.

DOI: 10.1002/adma.202202971

in electronics.^[11] Whereas homostructures are prevalent in conventional semiconductor electronics because of a distinct set of advantages (including ease of fabrication and reduced structural and electronic disorder), they have received comparatively little attention in oxide electronics. However, recent work on ferroelectric titanate homostructures^[12] has demonstrated that surprisingly complex vortex superstructures with noncollinear polar moments can emerge in structurally and chemically simple multilayer systems.

Motivated by these developments, we have used spin-polarized neutron reflectometry and diffraction to investigate the magnetic structure in $\text{La}_{1-x}\text{Sr}_x\text{MnO}_3$ (LSMO) homostructure arrays with alternating composition ($x = 0.4$ and 0.8). The phase diagram of bulk LSMO (Figure 1a)

has been the subject of numerous investigations especially in view of the “colossal” magnetoresistance in the ferromagnetic (FM) regime centered at $x \approx 0.3$, and ferromagnetic LSMO layers are one of the most common components of oxide heterostructures.^[1] Prior studies of LaMnO_3 – SrMnO_3 homostructures have uncovered thickness-induced metal–insulator transitions,^[13] spatially modulated ferromagnetism,^[14–16] and an enhancement of antiferromagnetic order compared to bulk LSMO.^[17] Our experiments on $\text{La}_{0.6}\text{Sr}_{0.4}\text{MnO}_3$ – $\text{La}_{0.2}\text{Sr}_{0.8}\text{MnO}_3$ homostructures with a comparatively small modulation of the doping level have uncovered complex magnetic “fan” superstructures without any analogue in bulk manganites, in qualitative analogy to the ferroelectric vortices in the titanates. These structures are characterized by emergent periodicity twice as large as the superlattice unit cell, analogous to synthetic antiferromagnetism in elemental superlattices,^[18] and are fully long-range ordered, despite the gradual variation of the doping level created by interdiffusion of Sr dopant ions. The high susceptibility of the noncollinear spin alignment to external magnetic fields holds promise for applications in the emerging field of noncollinear spintronics^[19] and for superconducting spin valves.^[20,21]

2. Results

LSMO homostructure arrays were grown by ozone-assisted molecular beam epitaxy. The Sr concentration was varied

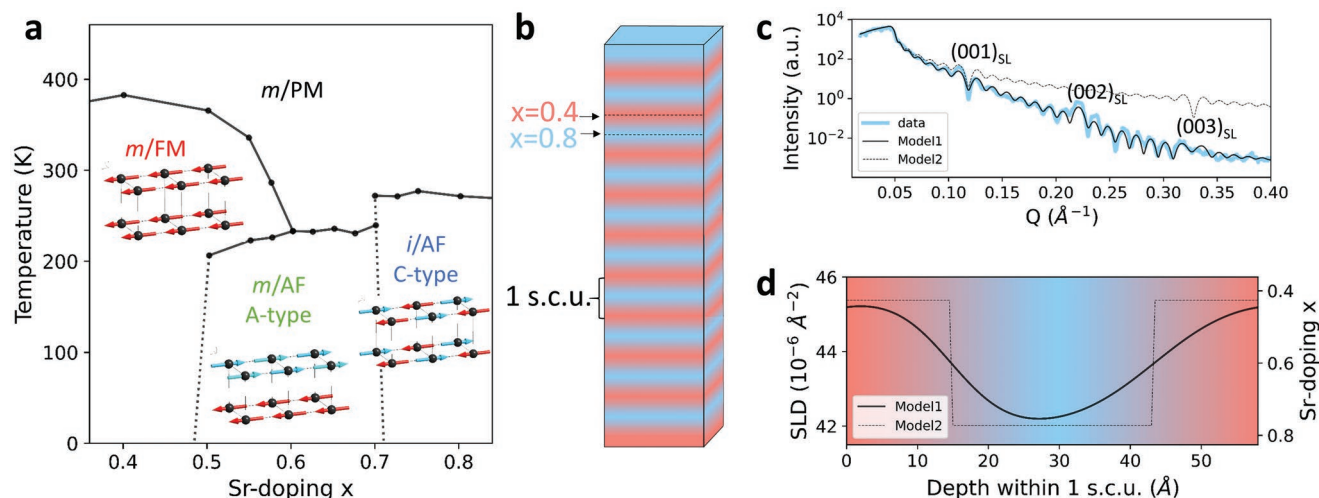


Figure 1. Phase diagram and structural characterization of LSMO homojunctions. a) Bulk phase diagram of $\text{La}_{1-x}\text{Sr}_x\text{MnO}_3$ with data points taken from ref. [22], where m/i stands for metallic/insulating, and PM/FM/AF indicate paramagnetic/ferromagnetic/antiferromagnetic phases. b) Schematic diagram of the SLs and definition of a s.c.u., where the zero is set in the center of the FM layer. c) Measured XRR profile of the sample N6 (light blue), best fit curve obtained with a Sr-diffusion model (black), and simulated curve assuming no Sr-diffusion (dashed black). d) SLD depth profile of one s.c.u. corresponding to the profiles with (solid black) and without (dashed black) Sr diffusion.

between the nominal values $x = 0.4$ (which in the bulk is a half-metallic ferromagnet) and overdoped $x = 0.8$ (an insulating C-type antiferromagnet, AF, in the bulk), as shown in Figure 1b. The thickness of the FM layer, d , was kept constant at 9 monolayers (MLs; 1 ML = 3.87 \AA), while the thickness of the AF layer was varied in the range of $n = 2$ –9 MLs. The supercell unit (s.c.u.) composed of the FM layer and the AF spacer was repeated ten times, with the exception of sample N6 which was repeated eight times. Throughout the article, we refer to the samples according to the thickness of their spacer layer; for instance, N6 denotes the sample with $n = 6$.

The superlattices (SLs) were initially characterized by X-ray structural depth profiling. Figure 1c shows a representative X-ray reflectivity (XRR) curve for sample N6. The main observation, common to all samples, is the presence of superstructural Bragg peaks, denoted as $(00n)_{\text{SL}}$, which arise from the periodic modulation of the Sr-concentration. Using a model-based fit, we obtain the depth profile of the scattering length density (SLD) shown as a solid line in Figure 1d. Comparison between two models with different values of interfacial diffusion clearly demonstrates the gradual change of the Sr-concentration between $x = 0.4$ and 0.8 (Figure 1c,d). The depth profile indicates Sr-diffusion with a characteristic length scale of 3–4 MLs ($\approx 15 \text{\AA}$).

Polarized neutron reflectometry (PNR) experiments were performed to study the depth dependent magnetic properties of the SLs through the detection and analysis of non-spin flip (NSF) and spin flip (SF) scattering in different magnetic fields H (see Experimental Section for details). Figure 2a displays a representative reflectivity curve of the sample N5 at the lowest temperature in the field-saturated state ($T = 3 \text{ K}$ and $H = 4.5 \text{ kOe}$). The strong superlattice Bragg peak $(001)_{\text{SL}}$ is a common feature of all samples. In contrast to XRR, however, it arises mostly from magnetic contrast rather than the modulation of the Sr concentration, which only results in a marginal ($<3\%$) modulation of the neutron SLD.

By fitting the PNR curves to a model that includes the nuclear SLD profile attained via XRR, we retrieve the magnetic depth profiles (Figure 2b). For the field-saturated sample, the magnetization along the applied magnetic field (M_x) shows a clear modulation, while the perpendicular component (M_y) is pinned to zero, indicating that the spins are fully aligned along the magnetic field direction, as shown by the black arrows in Figure 3a. The depth profile of M_x is asymmetric at the upper and lower interface, similar to prior observations.^[15] It is notable that the magnetization does not fall to zero at any depth, although no net magnetization is expected a priori in the center of the spacer layer, where the nominal doping $x = 0.8$ corresponds to C-type AF order.

The most striking feature was found at low fields ($H = 100 \text{ Oe}$) and intermediate temperatures ($T = 140 \text{ K}$), where a SF peak emerges at momentum transfer $Q \approx 0.055 \text{\AA}^{-1}$ (Figure 2c). Its momentum-space position, $(0 \ 0 \ \frac{1}{2})_{\text{SL}}$, indicates a period doubling of the magnetic structure. Since this feature appears exclusively in the SF channels, we can rule out the formation of a collinear synthetic ferri- or antiferromagnet. The corresponding magnetic SLD profile (Figure 2d) shows that the periodicity of the noncollinear component of the magnetization, M_y , is twice the periodicity of the collinear component M_x . The data thus imply a noncollinear magnetic structure where the spin directions of adjacent FM layers subtend an angle α (black arrows in Figure 3b).

Figure 4a compares the SF reflectivities of different samples at the same magnetic field and temperature. We observed $(0 \ 0 \ \frac{1}{2})_{\text{SL}}$ peaks in samples N5 and N6, but not in the other samples. This is in sharp contrast to the results from SQUID magnetometry, where all samples show a similar trend at intermediate temperatures (Figure S1a, Supporting Information), highlighting the unique ability of PNR to detect magnetic

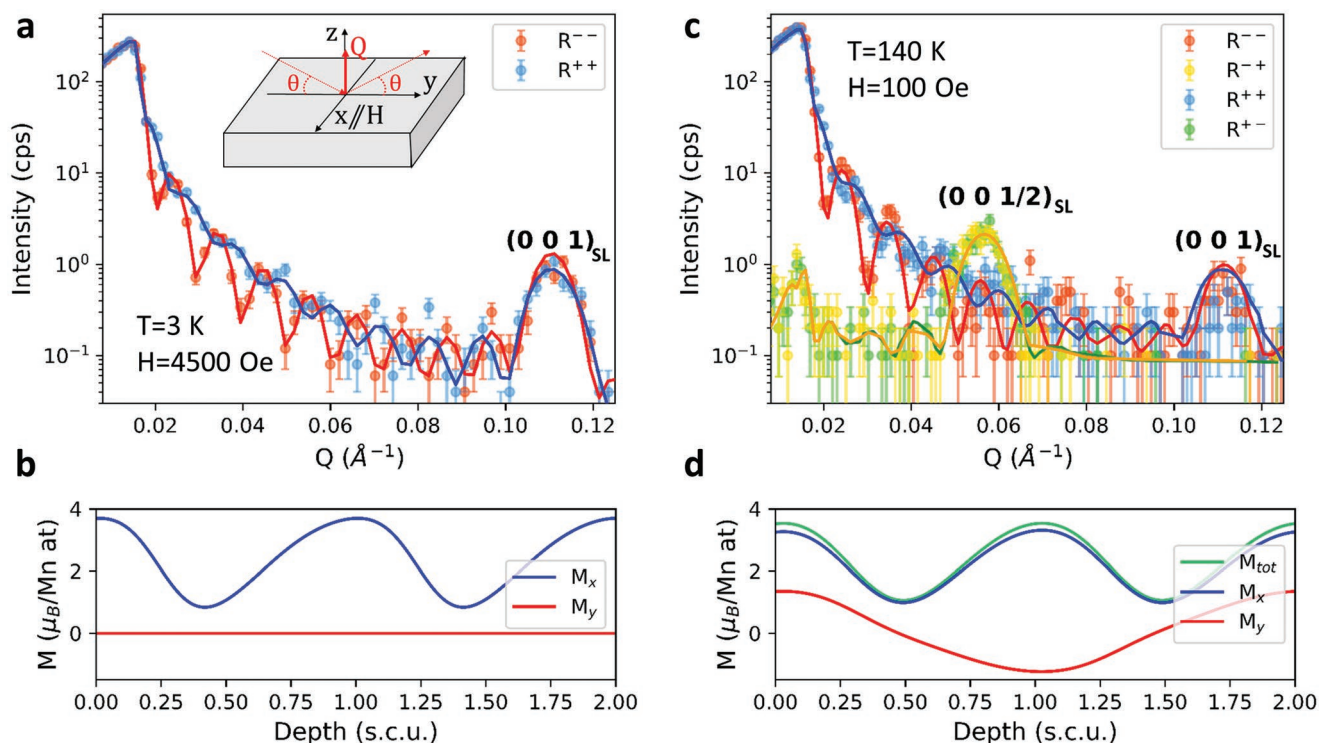


Figure 2. Selected PNR data for sample N5. a) PNR of N5 measured at temperature 3 K and in the saturation field of 4.5 kOe, together with the results of fits described in the text (solid lines). The SF channels, showing background signal only, are omitted. The inset shows a sketch of the coordinates used to describe the experimental setup. b) Magnetic depth profile over 2 s.c.u. at 3 K and 4.5 kOe, showing the component of magnetization M_x pointing along the applied field H (blue), and the component M_y perpendicular to H (red). c) PNR of sample N5 measured at $T=140$ K and $H=100$ Oe, together with fit curves (solid lines). d) Magnetic depth profile over 2 s.c.u. at 140 K and 100 Oe, showing the total magnetization profile (green), as well as M_x (blue) and M_y (red).

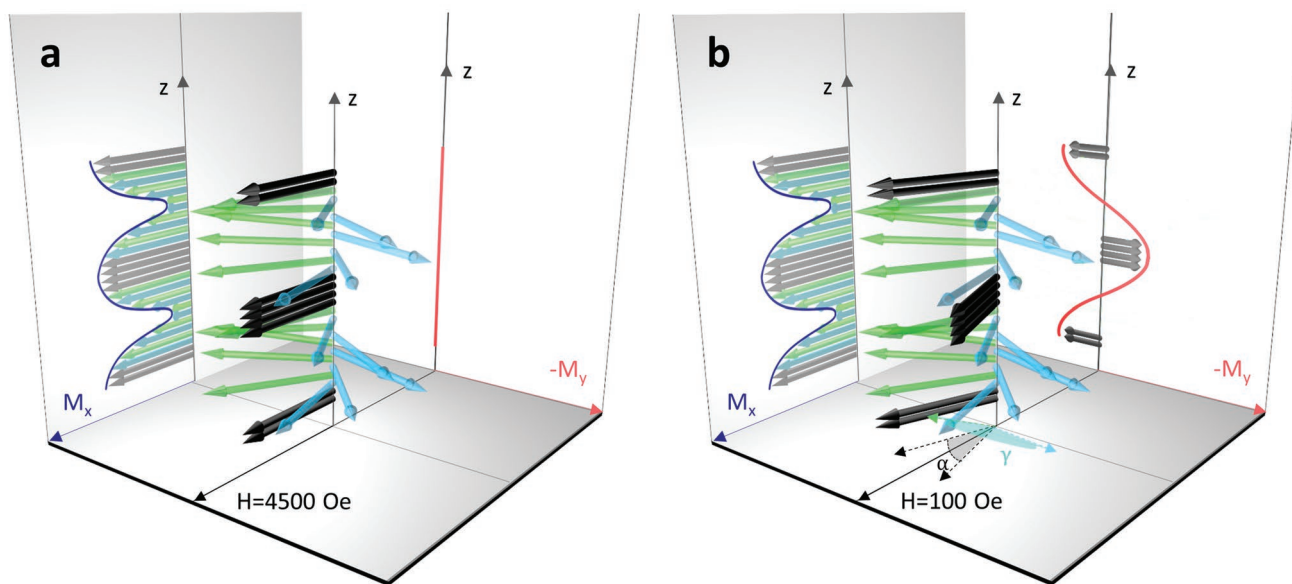


Figure 3. Visualization of the noncollinear magnetic structure. a) Model of the magnetic configuration in sample N5 at 3 K and 4.5 kOe. Each arrow represents the average magnetic moment direction of one ML, with black arrows indicating the FM layers, and green and blue arrows the canted AF spacer. The projections of the magnetic SLD profile parallel to the applied field M_x (perpendicular to the applied field M_y) are represented on the left (right) wall as blue (red) lines. b) Model of magnetic configuration in sample N5 at 140 K and 100 Oe, showing the doubling of the magnetic structure along the y -direction (red line). The definitions of the fan opening angle α and canting angle γ are shown as projections on the bottom plane.

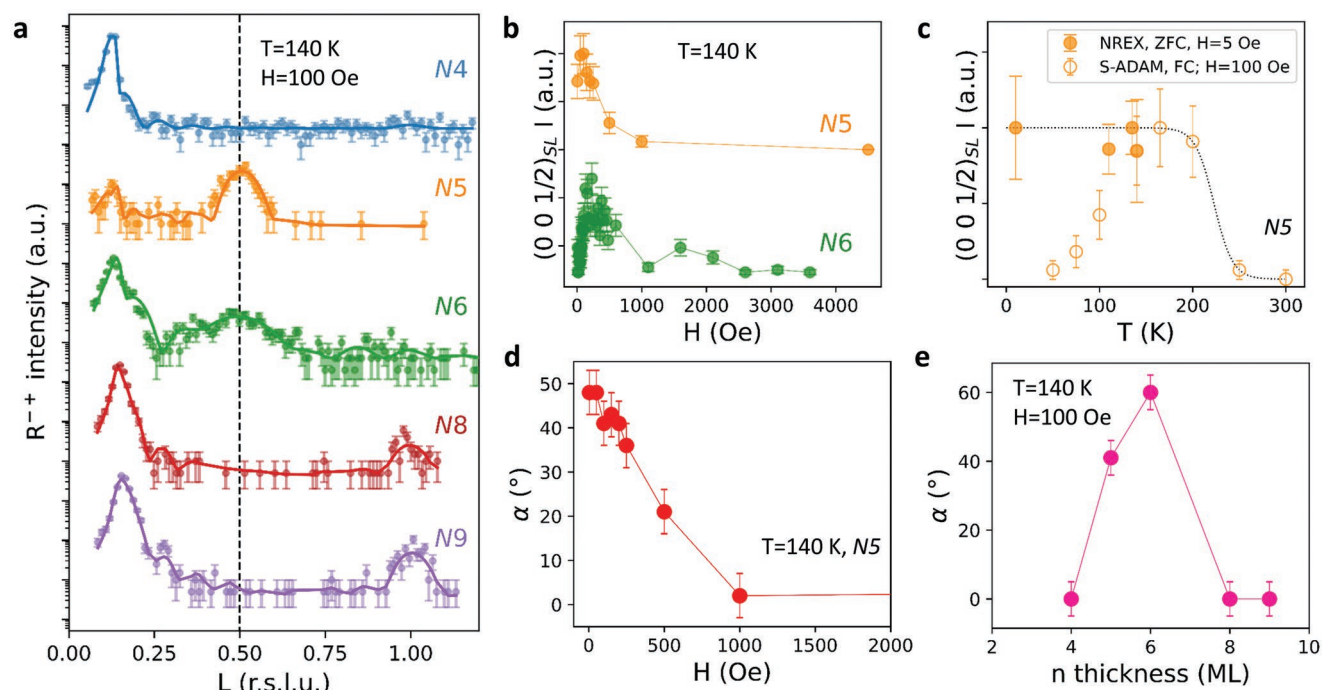


Figure 4. Characterization of the magnetic superstructure by PNR. a) SF channel measured on different samples at $T = 140$ K and $H = 100$ Oe, showing the emergence of the $(0\ 0\ \frac{1}{2})_{\text{SL}}$ peak for samples N5 and N6. The wave vector Q is quoted in reciprocal superlattice units. The curves are vertically shifted for clarity. The solid lines are the results of fits to a model based on stacked FM and AF units. b) Magnetic field dependence of the $(0\ 0\ \frac{1}{2})_{\text{SL}}$ peaks of samples N5 and N6. c) Temperature dependence of the $(0\ 0\ \frac{1}{2})_{\text{SL}}$ peak intensity of sample N5 after cooling in a field of 4.5 kOe (FC) and releasing the field to $H = 100$ Oe (empty circles), and after zero field cooling (ZFC) in a neutron guiding field of $H = 5$ Oe (full circles). Peak intensities in (b) and (c) are defined above background level and normalized to the maximum value found for sample N5. d) Field dependence of the opening angle α for N5. e) α versus overdoped layer thickness at 140 K and 100 Oe. The light lines in (b–e) are guides-to-the-eye.

superstructures. The shape of the $(0\ 0\ \frac{1}{2})_{\text{SL}}$ peak provides additional information on the correlation length of the superstructure. In sample N5, the peak width is identical to the other superstructure peaks, implying complete, long-range correlation between all FM layers. For N6, on the other hand, the peak is clearly broader, indicating a degradation of these correlations. PNR simulations suggest that only a part of this sample (5 out of 8 FM layers) is in the fan-like configuration (Figure S2, Supporting Information). The presence of uncorrelated FM layers is consistent with small steps observed in the hysteresis loop of N6 at 140 K (green points in Figure S1a, Supporting Information).

We now focus on sample N5 which displays the sharpest $(0\ 0\ \frac{1}{2})_{\text{SL}}$ peak. We find that the noncollinear structure is quite sensitive to external magnetic fields and shows a remarkable dependence on cooling history. The noncollinear alignment emerges spontaneously upon zero-field-cooling below $T_{\text{fan}} = 200$ K (Figure 4c). At $T = 140$ K, the SL peak intensity (Figure 4b) and the angle α extracted from the full PNR curves (Figure 4d) decrease continuously with increasing field, and a field-aligned collinear state is recovered for $H \gtrsim 1$ kOe. Field cooling below T_{fan} in 4.5 kOe and subsequent field release to 100 Oe also generates the noncollinear state, but only for temperatures above 100 K, where the macroscopic hysteresis loops show soft mag-

netism and small coercivity (Figure S1a, Supporting Information). For field cooling to lower temperatures, the collinear state is preserved even when the field is ramped to zero (Figure 4c). Finally, Figure 4e shows that the angle α at fixed field also depends sensitively on the thickness of the overdoped layer. The temperature, field, and composition dependence thus offer multifold tuning parameters for the magnetic structure.

3. Discussion

To fully elucidate the nature and origin of the magnetic superstructure, we first discuss the origin of the net magnetic moment in the AF spacer. PNR data on all SLs under saturation conditions (Figure S3, Supporting Information) show that the spacer magnetization approaches zero only for the thickest overdoped layers, in samples N8 and N9, while it remains nonzero for the remaining samples. This observation can be partially explained by the interdiffusion of dopants between $x = 0.4$ and 0.8 layers, which spreads out the Sr-concentration at the interface. However, chemical intermixing alone is insufficient to explain the nonzero magnetic moment of the spacer, because the SLD profile attained from XRR (see Figure S4, Supporting Information) indicates that the Sr-doping level at the center of the overdoped layer varies between $0.6 < x < 0.8$ for all samples. In bulk LSMO, the A- and

C-type AF order corresponding to these doping levels do not exhibit a net magnetization.

An additional effect that greatly influences the properties of oxide homo- and heterojunctions is the transfer of mobile charge carriers between adjacent layers.^[16,23,24] This effect is expected to drain holes from the overdoped spacer and to diminish its effective hole-doping, thus gradually transforming the nominally C-type AF (blue region in **Figure 5**) into an A-type AF state (green) and ultimately into a FM state (red) with decreasing thickness of the spacer. We can explain the reduced magnetic moment in the spacer of samples N5 and N6 if we assume a canting of moments in the A-type AF, as previously reported for both bulk manganites^[22] and thin films^[14,25] around $x \approx 0.5$ and attributed to competing double-exchange and superexchange interactions. The canting angle γ , defined as the angle between the moments of two adjacent MLs, was shown to depend on the Sr-doping level in thin films^[14] such that it varies between 0° (FM order) and 180° (AF order) for $0.4 < x < 0.6$.

To directly probe canted AF in the thin overdoped spacer, we have carried out reference measurements on a 50 nm-thick LSMO film with $x = 0.5$. Polarized neutron diffraction (PND) data at $T = 100$ K and $H = 5$ kOe revealed a pronounced peak at $Q = 0.83 \text{ \AA}^{-1}$ corresponding to the $(0 \ 0 \ \frac{1}{2})$ reflection of LSMO (**Figure 6a**). This peak emerges only in the SF channels, and thus signifies the perpendicular orientation of spins with respect to the applied field. The clear difference of the R^- and R^+ channels (**Figure 6b**) indicates the presence of a net moment,

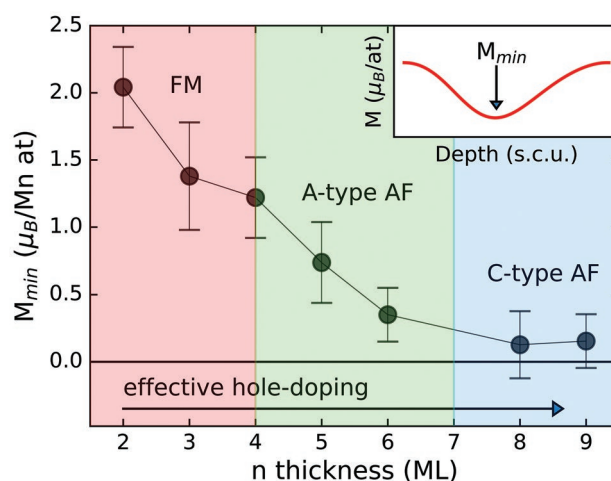


Figure 5. Magnetization in the center of the overdoped layer, retrieved from PNR data fitting, versus spacer thickness. Colors encode the dominant magnetic order of the spacer. The error bars correspond to a 5% increase in the figure of merit of the fit. Inset: Definition of M_{\min} in the magnetic depth profile.

directly confirming a canted AF state. Model simulations of this PNR curve allowed us to retrieve the net collinear component of $0.8 \mu_B/\text{Mn atom}$. Based on a total moment of $\approx 3.7 \mu_B/\text{Mn atom}$ corresponding to the $\text{Mn}^{3+}/\text{Mn}^{4+}$ ratio at $x = 0.5$,^[26] this translates into a canting angle $\gamma = 155^\circ$.

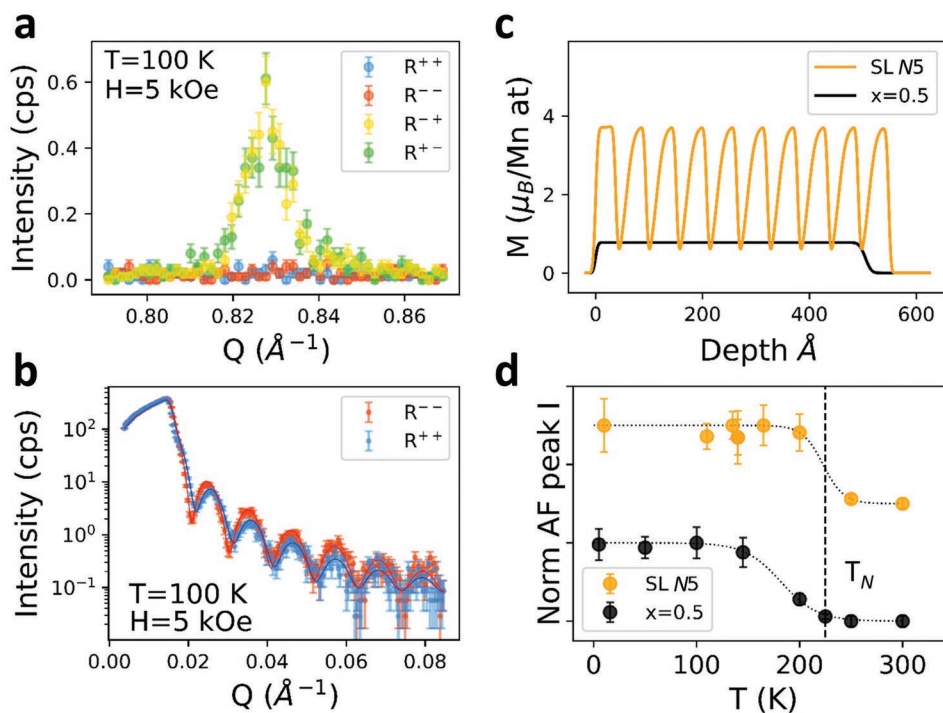


Figure 6. Reference measurements on the LSMO thin film with $x = 0.5$. a) AF peak measured by PND in the SF channel at $T = 100$ K and $H = 5$ kOe. b) PNR profiles at $T = 100$ K and $H = 5$ kOe, together with fit curves based on the magnetization profiles in (c). c) Comparison of magnetic depth profiles at $H = 5$ kOe of the N5 superlattice at $T = 140$ K and of the LSMO film at $T = 100$ K. d) Comparison of the temperature dependence of the normalized intensity of the $(0 \ 0 \ \frac{1}{2})_{\text{SL}}$ peak in N5 and of the $(0 \ 0 \ \frac{1}{2})$ peak in the LSMO reference film. The curves are vertically shifted for clarity. The dotted lines are guides-to-the-eye, the dashed line indicates the Néel temperature, T_N , of the LSMO film.

In Figure 6c, we compare the magnetic profile of the film with $x = 0.5$ and the SL N5 at the same temperature and magnetic field. The minimum value of M_x in N5 coincides with the one of the single layer, strongly suggesting the presence of a canted A-type AF state in the overdoped spacer of the SL. Additional evidence comes from the closely similar temperature dependences of the $(0\ 0\ \frac{1}{2})_{\text{SL}}$ reflection of the N5 sample and the $(0\ 0\ \frac{1}{2})$ reflection of the $x = 0.5$ layer (Figure 6d). In

particular, the close match between the Néel temperature of the AF film, $T_N \approx 225$ K, and the onset temperature of the fan structure, T_{fan} , in the SL underscores the common origin of both phenomena. Taken together, these findings imply that canted A-type antiferromagnetic correlations are present in the homojunctions, and that they are intimately related to the formation of the magnetic superstructure. Coupling between FM and AF layers via interfacial exchange interactions is expected on general grounds, because the A-type AF state is composed of monolayers that are ferromagnetically aligned in the SL plane. Such a coupling is consistent with a small negative exchange bias, which appears below 20 K after field cooling (Figure S1c, Supporting Information). In the absence of external magnetic fields, these interfacial interactions force the FM layers to follow the canted antiferromagnetism in the spacer layers, thus generating a period-two superstructure for spacer thicknesses for which the net coupling between adjacent FM layers is AF.

Figure 3 schematically illustrates the complete, fan-like spin arrangement of the N5 superlattice, comprising both canted FM and canted A-type AF correlations that are coupled by interfacial exchange interactions. The FM (canted AF) moments are represented by black (blue and green) arrows, respectively, and their amplitudes are assumed to be identical for simplicity. The AF region extends over the nominal thickness of 2–3 MLs at each interface of the spacer, consistent with the modulated profiles obtained from X-ray and neutron reflectometry. Following the observations of Santos et al.,^[14] we have assumed that the canting angle γ in the AF region varies in accordance with the Sr-profile, which implies $\gamma \approx 50^\circ$ at the interface with the FM layers and $\gamma \approx 155^\circ$ at the core of the spacer layer. Direct experimental information on the spatial variation of γ within the AF layer will have to await comprehensive PND measurements, which are outside the scope of the present study.

In the presence of a magnetic field, the additional Zeeman interaction leads to gradual tilting of the spins toward the field direction. The field dependence of the angle α (Figure 4d) can thus be understood as the result of competition between Zeeman and exchange interactions. This competition can be used as a tuning parameter for the noncollinearity of the fan structure, in contrast to the canted modulated spin structure found by Santos et al.^[14] which was shown to be stable up to at least 8.2 kOe. A similar tunable noncollinearity was reported for nickelate/manganite heterojunctions by Hoffman et al.,^[27] where the helical order in the nickelate spacers also leads to period-doubling of the magnetic structure. Remarkably, we have demonstrated that such complex long-range order can form in a homojunction array with a comparatively minor, gradual modulation of the doping level.

In sample N6, the canted-AF alignment of FM moments in adjacent supercells is only short-range ordered, and coexists with ferromagnetically aligned supercells (Figure S2d, Supporting Information), whereas the field-saturated state is completely ordered (Figure S2a, Supporting Information). The simplest mechanism for such a coexistence is a variation of the thickness of the canted-AF spacer layer across the sample, in combination with the delicate combination of exchange interactions that gives rise to the period-two superstructure. Indeed, the effective interfacial width extracted from XRR is somewhat larger in sample N6 than in most other samples (Figure S4, Supporting Information), possibly due to inhomogeneous broadening by 1–2 unit cells. However, we cannot rule out intrinsic mechanisms (such as magneto-static effects) promoting the coexistence of different magnetic supercell arrangements. In any case, the data on sample N6 indicate that the period-two superstructure is generic to homojunctions with intermediate spacer thickness, whereas those on sample N5 demonstrate that it can be stabilized uniformly over the full volume of a superlattice, despite its complex internal spin texture.

Based on these findings, we now discuss our observation that the magnetic superstructure is only present in samples with spacer thickness in the range $4 < n \leq 7$ (samples N5 and N6). In these samples, the overdoped layer hosts a canted A-type AF state, which induces the fan-like noncollinear order. For $n \leq 4$, on the other hand, the spacer thickness is smaller than the charge diffusion length, so that mobile charge carriers can leak into the spacer layer and enhance the FM double-exchange interaction. The entire SL thus behaves as a FM with slightly modulated magnetization. Finally, when $n \geq 8$, the overdoped layer presumably exhibits C-type AF, at least near its center which is well away from the interfaces (Figure 5). As this type of order exhibits antiferromagnetic correlations in the plane, there is no net coupling between adjacent FM layers so that a magnetic superstructure does not form.

4. Conclusions

We have discovered remarkably complex, highly noncollinear superstructures in a series of all-manganite homojunctions with modulated Sr concentration, and we have shown that these emergent structures can be long-range ordered despite the gradual variation of the doping level created by charge transfer and chemical intermixing. Analogous magnetic structures have been observed at interfaces of elemental rare earths and transition metals^[28] and at heterointerfaces of complex magnetic oxides,^[27,29–32] but their surprising appearance in simple homojunction arrays greatly lowers the barriers for their integration in electronic devices. We have also shown that the degree of noncollinearity is tunable via low magnetic fields, $H \lesssim 1$ kOe. With further development, oxide homojunctions may thus serve as powerful components of spintronic devices that rely on modulation of spin arrangements by external fields^[33] or spin-transfer torques.^[34] Epitaxial integration with oxide high-temperature superconductors will further expand the range of possible applications, for instance as all-oxide triplet spin-valve structures in superconducting spintronics.^[35–37]

5. Experimental Section

Synthesis: Ozone assisted molecular beam epitaxy was used to grow homostructures of nominal composition $10\times [\text{La}_{0.6}\text{Sr}_{0.4}\text{MnO}_3(d)+\text{La}_{0.2}\text{Sr}_{0.8}\text{MnO}_3(n)]$, where d and n are the number of monolayers (MLs) for the different building blocks, on $(\text{LaAlO}_3)_{0.3}(\text{SrAl}_{0.5}\text{O}_3)_{0.7}$ (LSAT) substrates of dimensions $10\times 10\text{ mm}^2$. The substrates were annealed at 630°C for 30 min in an (O_2+O_3) atmosphere with a pressure of 1.7×10^{-5} Torr. The same temperature and pressure were maintained during growth. The substrate temperature was measured by a radiation pyrometer with wavelength $8\text{--}14\text{ }\mu\text{m}$, and the (O_2+O_3) pressure was measured with a residual gas analyzer. To control the thickness and crystallinity of the epitaxial layers, the layer-by-layer deposition was monitored in situ by reflection high energy electron diffraction (RHEED) (Figures S5 and S6, Supporting Information). The high quality of the substrates and the absence of Sr-segregation after the annealing were confirmed by RHEED images taken prior to the deposition (Figures S5a and S6a, Supporting Information).

Characterization: The lattice structure was characterized at room temperature by X-ray reflectometry at the KARA synchrotron in Karlsruhe, Germany, with wavelength $1.238\text{ }\text{\AA}$. The magnetic properties of the SLs were studied between 5 and 295 K by SQUID-VSM magnetometry, using a MPMS3 magnetometer (Quantum Design). The magnetic field was applied in the SL plane.

Neutron Reflectometry and Diffraction: The PNR measurements were carried out on the angle-dispersive neutron reflectometers NREX^[38] in Garching, Germany, and Super-ADAM^[39] in Grenoble, France. Using different configurations of spin polarizers, spin flippers, and analyzers, SF neutrons were detected in the channels R^+ and R^- , and NSF neutrons in the R^- and R^{++} . The indices \pm indicated the polarization of the neutron spin before and after the reflection. Nonmagnetic scattering was detected in the R^{++} and R^- channels, magnetic scattering from moments aligned parallel to the external field H was detected as the difference between R^{++} and R^- , and moments transverse to H were detected in the R^{++} and R^+ channels. The coordinates used to describe the experimental geometry were defined as shown in the inset of Figure 2a, with z normal to the surface of the film, and x and y parallel to the surface. A closed-cycle cryostat was used at NREX, and a continuous-flow cryostat was used at Super-ADAM to generate temperatures in the range between 3 and 300 K. Magnetic fields between 5 and 5000 Oe were applied in-plane along the x -direction. All PNR and XRR curves were analyzed with the GenX software.^[40] The Super-ADAM reflectometer was also used for polarized neutron PND measurements, where the $(0\ 0\ \frac{1}{2})$ reflections of the A-type AF order in a LSMO thin film were detected, in the same field and temperature conditions as described above.

Statistical Analysis: The PNR and XRR data were normalized to the counting time. The error bars of these data corresponded to the standard deviation of the count rate. The PNR and XRR data were fitted by numerically minimizing the logarithmic-difference figure of merit.^[40] The error bars of the fit parameters were estimated via a 5% increase of the figure of merit.

Supporting Information

Supporting Information is available from the Wiley Online Library or from the author.

Acknowledgements

This work is partially based on experiments performed at the NREX instrument operated by the Max-Planck Society at the Heinz Maier-Leibnitz Zentrum (MLZ), Garching, Germany. The authors would like to thank the ILL for the allocation of neutron time at Super-ADAM. The authors acknowledge the help of Reiner Mueller in the creation of the

graphic model for Figure 3a,b. The KIT Institute for Beam Physics and Technology (IBPT) is acknowledged for the operation of the storage ring Karlsruhe Research Accelerator (KARA), and for provision of beamtime at the KIT light source. L.G., Y.K., T.K., and B.K. acknowledge financial support of the German Research Foundation (Deutsche Forschungsgemeinschaft, DFG, Project No. 107745057-TRR80).

Open access funding enabled and organized by Projekt DEAL.

Conflict of Interest

The authors declare no conflict of interest.

Data Availability Statement

The data that support the findings of this study are available from the corresponding author upon reasonable request.

Keywords

interfacial exchange coupling, magnetic fan structures, manganite superlattices, noncollinear magnetism, synthetic antiferromagnets

Received: April 1, 2022

Revised: June 27, 2022

Published online: July 29, 2022

- [1] H. Hwang, Y. Iwasa, M. Kawasaki, B. Keimer, N. Nagaosa, Y. Tokura, *Nat. Mater.* **2012**, *11*, 103.
- [2] G. Kim, Y. Khayduk, M. Bluschke, Y. E. Suyolcu, G. Christiani, K. Son, C. Dietl, T. Keller, E. Weschke, P. A. van Aken, G. Logvenov, B. Keimer, *Phys. Rev. Mater.* **2019**, *3*, 084420.
- [3] M. Gibert, P. Zubko, R. Scherwitzl, J. Iniguez, J. Triscone, *Nat. Mater.* **2012**, *11*, 195.
- [4] H. Bhatt, Y. Kumar, C. L. Prajapat, C. J. Kinane, A. Caruana, S. Langridge, S. Basu, S. Singh, *Adv. Mater. Interfaces* **2020**, *7*, 2001172.
- [5] D. Yi, J. Liu, S. Hsu, L. Zhang, Y. Choi, J. Kim, Z. Chen, J. D. Clarkson, C. R. Serrao, E. Arenholz, P. J. Ryan, H. Xu, R. J. Birgeneau, R. Ramesh, *Proc. Natl. Acad. Sci. USA* **2016**, *113*, 6397.
- [6] D. Yi, C. L. Flint, P. P. Balakrishnan, K. Mahalingam, B. Urwin, A. Vailionis, A. T. N'Diaye, P. Shafer, E. Arenholz, Y. Choi, K. H. Stone, J. Chu, B. M. Howe, J. Liu, I. R. Fisher, Y. Suzuki, *Phys. Rev. Lett.* **2017**, *119*, 077201.
- [7] J. Stahn, J. Chakhalian, C. Niedermayer, J. Hoppler, T. Gutberlet, J. Voigt, F. Treubel, H.-U. Habermeier, G. Christiani, B. Keimer, C. Bernhard, *Phys. Rev. B* **2005**, *71*, 140509.
- [8] M. A. Uribe-Laverde, D. K. Satapathy, I. Marozau, V. K. Malik, S. Das, K. Sen, J. Stahn, A. Rühm, J.-H. Kim, T. Keller, A. Devishvili, B. P. Toperverg, C. Bernhard, *Phys. Rev. B* **2013**, *87*, 115105.
- [9] J.-H. Kim, I. Vrejoiu, Y. Khayduk, T. Keller, J. Stahn, A. Rühm, D. K. Satapathy, V. Hinkov, B. Keimer, *Phys. Rev. B* **2012**, *86*, 180402.
- [10] J. Chakhalian, J. W. Freeland, A. J. Millis, C. Panagopoulos, J. M. Rondinelli, *Rev. Mod. Phys.* **2014**, *86*, 1189.
- [11] M. Coll, J. Fontcuberta, M. Althammer, M. Bibes, H. Boschker, A. Calleja, G. Cheng, M. Cuoco, R. Dittmann, B. Dkhil, I. El Baggari, M. Fanciulli, I. Fina, E. Fortunato, C. Frontera, S. Fujita, V. Garcia, S. Goennenwein, C.-G. Granqvist, J. Grollier, R. Gross, A. Hagfeldt, G. Herranz, K. Hono, E. Houwman, M. Huijben, A. Kalaboukhov, D. Keeble, G. Koster, L. Kourkoutis, et al., *Appl. Surf. Sci.* **2019**, *482*, 1.

- [12] A. K. Yadav, C. T. Nelson, S. L. Hsu, Z. Hong, J. D. Clarkson, C. M. Schlepütz, A. R. Damodaran, P. Shafer, E. Arenholz, L. R. Dedon, D. Chen, A. Vishwanath, A. M. Minor, L. Q. Chen, J. F. Scott, L. W. Martin, R. Ramesh, *Nature* **2016**, 530, 198.
- [13] A. Bhattacharya, S. J. May, S. G. E. te Velthuis, M. Warusawithana, X. Zhai, B. Jiang, J.-M. Zuo, M. R. Fitzsimmons, S. D. Bader, J. N. Eckstein, *Phys. Rev. Lett.* **2008**, 100, 257203.
- [14] T. S. Santos, B. J. Kirby, S. Kumar, S. J. May, J. A. Borchers, B. B. Maranville, J. Zarestky, S. G. E. te Velthuis, J. van den Brink, A. Bhattacharya, *Phys. Rev. Lett.* **2011**, 107, 167202.
- [15] S. J. May, A. B. Shah, S. G. E. te Velthuis, M. R. Fitzsimmons, J. M. Zuo, X. Zhai, J. N. Eckstein, S. D. Bader, A. Bhattacharya, *Phys. Rev. B* **2008**, 77, 174409.
- [16] M. Keunecke, F. Lyzwa, D. Schwarzbach, V. Roddatis, N. Gauquelin, K. Müller-Caspary, J. Verbeeck, S. J. Callori, F. Klose, M. Jungbauer, V. Moshnyaga, *Adv. Funct. Mater.* **2020**, 30, 1808270.
- [17] S. J. May, P. J. Ryan, J. L. Robertson, K. J.-W., T. S. Santos, E. Karapetrova, J. Zarestky, X. Zhai, S. G. E. te Velthuis, J. N. Eckstein, S. D. Bader, A. Bhattacharya, *Nat. Mater.* **2009**, 8, 892.
- [18] S. S. P. Parkin, N. More, K. P. Roche, *Phys. Rev. Lett.* **1990**, 64, 2304.
- [19] P. Qin, H. Yan, X. Wang, Z. Feng, H. Guo, X. Zhou, H. Wu, X. Zhang, Z. Leng, H. Chen, Z. Liu, *Rare Met.* **2020**, 39, 95.
- [20] Y. Fominov, A. Golubov, T. Karminskaya, M. Y. Kupriyanov, R. G. Deminov, L. R. Tagirov, *JETP Lett.* **2010**, 91, 308.
- [21] V. I. Zdravkov, J. Kehrle, G. Obermeier, D. Lenk, H.-A. Krug von Nidda, C. Müller, M. Y. Kupriyanov, A. S. Sidorenko, S. Horn, R. Tidecks, L. R. Tagirov, *Phys. Rev. B* **2013**, 87, 144507.
- [22] J. Hemberger, A. Krimmel, T. Kurz, H.-A. Krug von Nidda, V. Y. Ivanov, A. A. Mukhin, A. M. Balbashov, A. Loidl, *Phys. Rev. B* **2002**, 66, 094410.
- [23] T. Koida, M. Lippmaa, T. Fukumura, K. Itaka, Y. Matsumoto, M. Kawasaki, H. Koinuma, *Phys. Rev. B* **2002**, 66, 144418.
- [24] A. Glavic, H. Dixit, V. R. Cooper, A. A. Aczel, *Phys. Rev. B* **2016**, 93, 140413.
- [25] T. S. Santos, S. J. May, J. L. Robertson, A. Bhattacharya, *Phys. Rev. B* **2009**, 80, 155114.
- [26] O. Chmaissem, B. Dabrowski, S. Kolesnik, J. Mais, J. D. Jorgensen, S. Short, *Phys. Rev. B* **2003**, 67, 094431.
- [27] J. D. Hoffman, B. J. Kirby, J. Kwon, G. Fabbri, D. Meyers, J. W. Freeland, I. Martin, O. G. Heinonen, P. Steadman, H. Zhou, C. M. Schlepütz, M. P. M. Dean, S. G. E. te Velthuis, J.-M. Zuo, A. Bhattacharya, *Phys. Rev. X* **2016**, 6, 041038.
- [28] T. D. C. Higgs, S. Bonetti, H. Ohldag, N. Banerjee, X. L. Wang, A. J. Rosenberg, Z. Cai, J. H. Zhao, K. A. Moler, J. W. A. Robinson, *Sci. Rep.* **2016**, 6, 30092.
- [29] K. R. Nikolaev, A. Y. Dobin, I. N. Krivorotov, W. K. Cooley, A. Bhattacharya, A. L. Koblinskii, L. I. Glazman, R. M. Wentzovitch, E. D. Dahlberg, A. M. Goldman, *Phys. Rev. Lett.* **2000**, 85, 3728.
- [30] W. Lü, S. Saha, X. Wang, X. R. Wang, Z. Q. Liu, K. Gopinadhan, A. Annadi, S. W. Zeng, Z. Huang, B. C. Bao, C. X. Cong, M. Venkatesan, T. Yu, J. M. D. Coey, Ariando, T. Venkatesan, *Nat. Commun.* **2016**, 7, 11015.
- [31] B. Chen, H. Xu, C. Ma, S. Mattauch, D. Lan, F. Jin, Z. Guo, S. Wan, P. Chen, G. Gao, F. Chen, Y. Su, W. Wu, *Science* **2017**, 357, 191.
- [32] M. Gibert, M. Viret, P. Zubko, N. Jaouen, J.-M. Tonnerre, A. Torres-Pardo, S. Catalano, A. Gloter, O. Stéphan, J.-M. Triscone, *Nat. Commun.* **2016**, 7, 11227.
- [33] J. D. Hoffman, S. M. Wu, B. J. Kirby, A. Bhattacharya, *Phys. Rev. Appl.* **2018**, 9, 044041.
- [34] A. Brataas, G. E. Bauer, P. J. Kelly, *Phys. Rep.* **2006**, 427, 157.
- [35] Y. Kalcheim, T. Kirzhner, G. Koren, O. Millo, *Phys. Rev. B* **2011**, 83, 064510.
- [36] C. Visani, Z. Sefrioui, J. Tornos, C. Leon, J. Briatico, M. Bibes, A. Barthélémy, J. Santamaría, J. E. Villegas, *Nat. Phys.* **2012**, 8, 539.
- [37] Y. N. Khaydukov, G. A. Ovsyannikov, A. E. Sheyerman, K. Y. Constantinian, L. Mustafa, T. Keller, M. A. Uribe-Laverde, Y. V. Kisinskii, A. V. Shadrin, A. Kalaboukhov, B. Keimer, D. Winkler, *Phys. Rev. B* **2014**, 90, 035130.
- [38] Y. Khaydukov, O. Soltwedel, T. Keller, *J. Large-Scale Res. Facil.* **2015**, 1, A38.
- [39] A. Devishvili, K. Zhernenkov, A. J. C. Dennison, B. P. Toperverg, M. Wolff, B. Hjörvarsson, H. Zabel, *Rev. Sci. Instrum.* **2013**, 84, 025112.
- [40] M. Björck, G. Andersson, *J. Appl. Crystallogr.* **2007**, 40, 1174.